

## LIGHT SCATTERING FROM A DROP WITH AN EMBEDDED FLAKE: APPLICATION TO THE TIME-SHIFT TECHNIQUE

Lingxi Li<sup>1, 2\*</sup>, Simon Rosenkranz<sup>2</sup>, Walter Schäfer<sup>2</sup>, Cameron Tropea<sup>1</sup>

<sup>1</sup>Technische Universität Darmstadt, Institute of Fluid Mechanics and Aerodynamics, Alarich-Weiss-Strasse 10, 64287 Darmstadt, Germany

<sup>2</sup>AOM-Systems GmbH, Flughafenstrasse 15, 64347 Griesheim, Germany  
(\* ) li@sla.tu-darmstadt.de

### Abstract

This study is devoted to computing the light scattering from drops with an embedded, reflecting flake, as encountered with metallic paints. Such drops are typical in the automotive industry and a complete knowledge of scattering characteristics is a prerequisite to optically measuring the drop size and velocity and to determine whether the drop contains a flake or not. The light scattering is computed using a ray tracing method. Once the light scattering has been computed, this information can be used to simulate the response of specific instruments. In the present case the signal generation of a time-shift instrument has been exemplary studied.

Keywords: light scattering, Gaussian beam, ray tracing, time-shift technique

### 1. Introduction

Atomization in the automotive paint industry must deal with a large variety of different paints, according to customer desires. Maintaining quality of the coating finish is therefore closely related to good control of atomization under varying conditions of viscosity, surface tension and pigment composition. Typical of automotive painting is a metallic finish, achieved using aluminium flakes dispersed into the paint. Upon atomization however, not all drops contain such flakes and there is considerable interest from industry to know what percentage of drops contain flakes and whether a correlation exists between size and flake presence. For this, a measurement technique is required and the present study is motivated by the possibility of achieving such a measurement using optical means. Thus, the goal is to measure not only size and velocity of individual drops in a spray, but also the existence of a reflecting aluminium flake.

Attention is first directed towards computing the light scattered from such a drop with an embedded flake, since this capability is a pre-requisite to studying the response of any optical measurement instrument. Theoretical solutions of light scattering with such arbitrary boundary conditions (size and orientation of flake in the drop) are not available and any numerical approach such as the T-matrix [6] or FDTD methods [14] are severely limited to very small sizes. Therefore, in the present study, an approach based on ray tracing is adopted, similar to that used in [8][13]. In anticipation of using the light scattering results for studying instrument response, the incident light is considered to be a Gaussian beam, with the drop arbitrarily positioned within. Thus, each ray to be traced is characterised by a starting amplitude and direction. The phase of each ray is not preserved in this simulation of light scattering as in [15]; hence, interference effects cannot be reproduced. However, the polarization is preserved, essential for capturing the intensity of the transmitted and reflected intensities at each interface encountered on its path through the drop.

Once the light scattering has been computed and verified by comparison to simpler situations offering theoretical solutions, the signal generation of a time-shift instrument is simulated. These synthetic signals, well defined for given drop and flake characteristics (size, position, orientation, refractive index), can be used to devise suitable signal processing algorithms for flake detection for this instrument. This simulation of light scattering is not suitable to reproduce signals as would be expected from a phase Doppler interferometer, since the phase of each ray is not computed.

### 2. Description of the laser beam

Already upon defining the incident beam, characteristics typical of a time-shift instrument have been used, for instance the Spray-Spy instrument from AOM-Systems [2]. In this case the laser beam has a beam waist of 1 mm in the X direction and a beam waist of 10  $\mu\text{m}$  in the Y direction. Such a non-circular Gaussian beam (light sheet) is used to im-

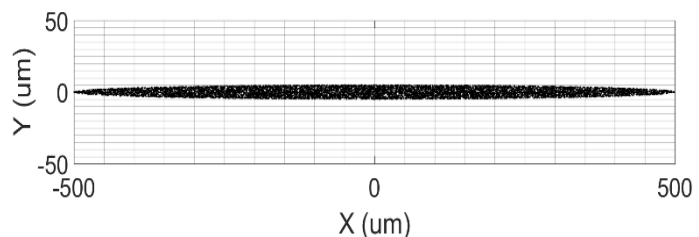


Figure 1: Randomly generated starting points for the ray tracing.

prove the directional sensitivity of the instrument, as described in [1]. This non-circular Gaussian beam is treated as a bundle of rays. The properties of each ray are first specified, such as the starting point, propagation direction, and the initial amplitude of the electric field  $E_0$ . The starting points of the large number of beams used in the simulation are randomly distributed in space. This is similar to the approach used in [13] and experience confirms that convergence of the computed light scattering diagrams is achieved with much fewer rays than if a regular grid spacing is used for the starting points. Figure 1 illustrates exemplarily the starting points of such a beam, showing the transverse plane of rays for the focussed non-circular Gaussian beam.

For a non-circular Gaussian laser beam, the complex amplitude can be described as [11].

$$E(\mathbf{r}, z) = E_0(z) \exp \left[ -i\phi_{ac} + i\eta(z) - ik \left( \frac{x^2}{2q_1(z)} + \frac{y^2}{2q_2(z)} \right) \right] \quad (1)$$

where  $\phi_{ac}$  is the phase accumulated from the chosen reference point.  $\mathbf{r}$  is the transversal vector, which is a function of  $(x, y)$ ; the  $q$  parameter is obtained from the following equation [7]:

$$\frac{1}{q_n(z)} = \frac{1}{R(z)} - i \frac{\lambda}{\pi \omega_n^2(z)}, n = 1, 2; \quad (2)$$

where  $w_i$  is the principle semi-axis of the light spot ellipse and  $R(z)$  is the principle radii of curvature of the wavefront. The Gouy phase  $\eta(z)$  can be expressed with the following equation [3]:

$$\eta(z) = \frac{1}{2} \left[ \tan^{-1} \left( \frac{z - z_{01}}{Z_{R1}} \right) + \tan^{-1} \left( \frac{z - z_{02}}{Z_{R2}} \right) \right] \quad (3)$$

where  $z_{01}$  is the position of beam waist in the  $X$  direction and  $Z_{R1}$  is the Rayleigh range.

For the time shift technique, the measurement volume is in the Rayleigh range of the laser beam, so the propagation direction for all initial rays will be treated as constant.

### 3. Description of the drop and the embedded flake

The physical properties of the drop, such as the refractive index  $n_t$  and the radius  $R$ , are specified. For the simulation, the drop is treated as a sphere, which can be expressed as

$$\frac{(x - x_0)^2}{R^2} + \frac{(y - y_0)^2}{R^2} + \frac{(z - z_0)^2}{R^2} = 1 \quad (4)$$

whereby the coordinate system is pictured in Figure 2. A flake inside the drop is treated as a flat disc, with the flake center at some  $(x, y, z)$  coordinate, with radius  $r$  and the surface normal  $\vec{n}$ . The surface normal is a vector with the zenith angle  $\alpha$  and azimuthal angle  $\beta$  also shown in Figure 2. Using the zenith and azimuthal angles, the normal vector of the flake can be described as [9]:

$$\vec{n} = \begin{pmatrix} n1 \\ n2 \\ n3 \end{pmatrix} = \begin{pmatrix} \mathbf{e}_x \cdot \mathbf{n}1 \\ \mathbf{e}_y \cdot \mathbf{n}2 \\ \mathbf{e}_z \cdot \mathbf{n}3 \end{pmatrix} = \begin{pmatrix} \sin \alpha \cdot \cos \beta \\ \sin \alpha \cdot \sin \beta \\ \cos \alpha \end{pmatrix} \quad (5)$$

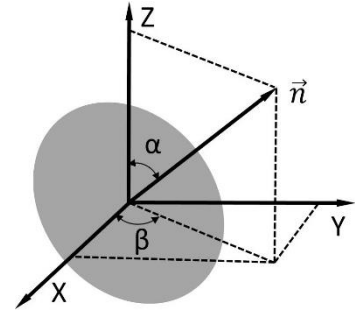


Figure 2: Description of the normal vector of the flake in Cartesian coordinate system.

### 4. Ray tracing algorithm and validation

For the present study the ray tracing algorithm first checks whether a given ray intersects with the drop. The incident beam is non-circular and Gaussian and the drop can be arbitrarily placed in the ray, so an intersection does not always occur. If however the ray intersects the drop, then the intersection point on the drop surface is calculated. The direction of the reflected ray and refracted ray at each interface intersection is computed using Snell's law and the amplitude of the electric field is given by the Fresnel equations for the reflected and refracted (transmitted) rays [5]. For each ray, the computation for one scattering order is followed by the computation for the next scattering order, based on the computational results up to that stage. This process is repeated until the computation for all scattering orders of all rays is complete. The information of all rays is saved. To compute a scattering diagram a point detector, defined using a solid scattering angle of 0.0029 sr, is traced through 0 to 180°. At each position, the intensity of the scattered light (Eq. (6)) is given as the sum over the intensity of all rays falling onto the detector (Eq. (7)) [13]:

$$I_k = \frac{c}{2} |E|^2 \quad (6)$$

$$I_{total}(\theta_i, \varphi_j) = \sum_{k=1}^m I_k \quad (7)$$

To validate the code, simulation results for a plane wave have been compared with the known Lorenz-Mie solution [10]. The drop is a transparent drop of relative refractive index  $m$  and no flake is present. As an example validation, Figure 3 illustrates the scattering diagram of the first five scattering orders for a 50 $\mu\text{m}$  drop, compared with the results from a Lorenz-Mie computation, invoking also a Debye series decomposition [4] to examine the agreement between individual scattering orders. In general the agreement is good, exhibiting the expected deviations arising from the geometric optics approach of ray tracing. The interference phenomena in the rainbows is not captured and neither is the effect of surface waves captured, evident especially in the scattering of first-order refraction at angles beyond about 85 degrees. Diffraction in forward scatter is not included in the ray tracing algorithm. Nevertheless, the ray tracing exhibits very good agreement for the first three scattering orders and is suitable for analyzing the signal generation of the time-shift technique.

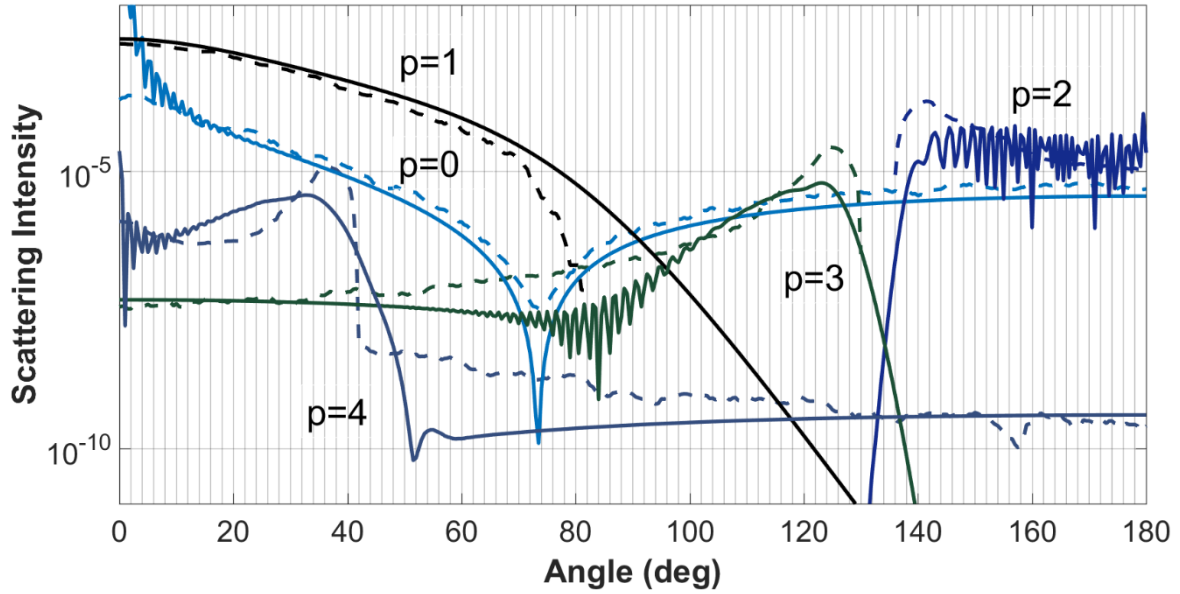


Figure 3: Comparison between Lorenz-Mie theory with Debye series decomposition (solid lines) and ray tracing (dashed lines): drop diameter=100 $\mu\text{m}$ ,  $n_r=1.343$ .

Further validation is performed for the case of a flake embedded in the drop. Such a circular flake (disk) is shown in Figure 4, in which the flake is centered in the drop and orientated parallel to the Y direction. In this study the flakes are perfectly reflecting disks of zero thickness.

In such a position, rays transmitted into the drop will be blocked once the incident ray becomes too close to the Z-axis; hence, the forward scattering of the first scattering order will be affected. As Figure 5 shows in the scattering diagram for the first scattering order, part of the forward scattering is lost. This condition of blocking of the ray internally in the drop is parameterized using the angle of the incident ray at the initial intersection point,  $\theta_i$ , and the resulting exit angle of first-order refraction,  $\theta_b$ . Referring to the diagram shown in Figure 4, an explicit expression for the blocking angle  $\theta_b$  can be obtained and this angle is shown in Figure 5 as a dashed line:

$$\frac{r}{\sin \theta_t} = \frac{R}{\sin(0.5 * \pi + \sin^{-1}(\sin \theta_t * nt) - \theta_t)} \quad (8)$$

$$\theta_b = 2 * (\theta_i - \theta_t) \quad (9)$$

Note also in Figure 5 that with a flake, an additional contribution of first-order refraction appears in backscatter, i.e. for scattering angles large than about 150 deg. This corresponds to the rays which have been blocked and reflected from the surface of the flake.

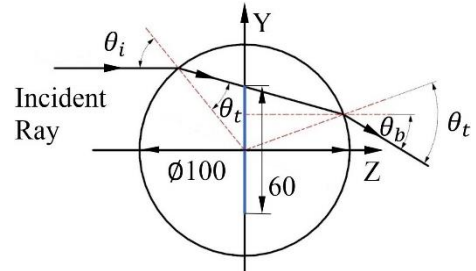


Figure 4: Disk positioned inside the drop can block the transmission of some rays: drop diameter=100 $\mu\text{m}$ , flake diameter=60 $\mu\text{m}$ , zenith angle  $\alpha=0$  deg, azimuthal angle  $\beta=0$  deg,  $n_r=1.343$ .

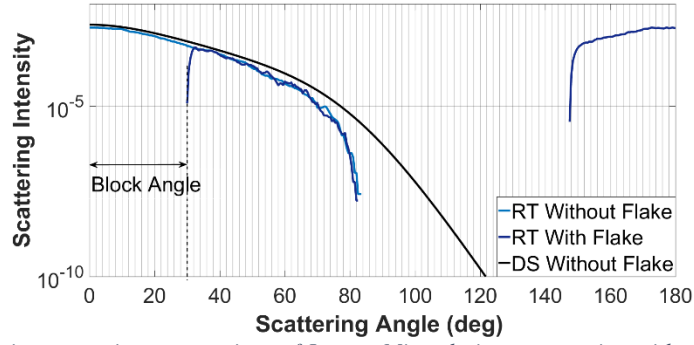


Figure 5: First-order refraction scattering: comparison of Lorenz-Mie solution, ray tracing without flake, ray tracing with flake: drop diameter=100 $\mu$ m, flake diameter=60 $\mu$ m, zenith angle  $\alpha = 0$  deg, azimuthal angle  $\beta = 0$  deg,  $n_1 = 1.343$ , RT – Ray Tracing, DS – Debye Series

## 5. The time-shift technique and signal generation

The time-shift technique, which is also known as the pulsed-displacement technique, is a method to measure size, velocity, and relative refractive index ( $m$ ) of spherical particles. As Figure 6 shows, a detector placed in the backscatter direction (e.g. 150°) will register a time dependent signal comprising several peaks, corresponding to the different scattering orders as a transparent particle passes through a shaped beam. Details about the measurement principle and optical design can be found in [1][12].

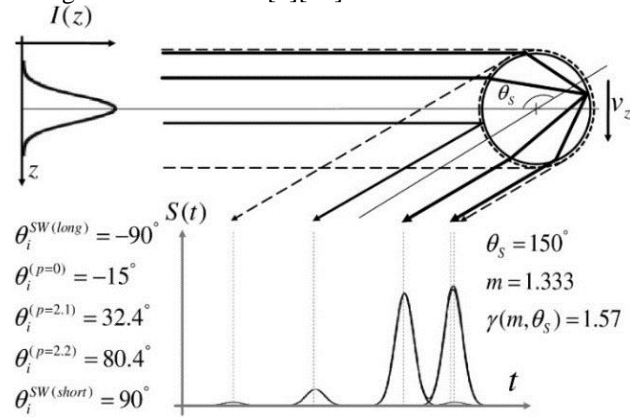


Figure 6: Principle of time-shift measurement technique [12].  $p$  designates the scattering order, according to how many paths occur internal to the drop [12].  $\theta$  expresses the angle of the incident point for each scattering order. SW designates surface waves.

To compute the signal arising from the passage of a drop through the focused beam of a time-shift instrument, first a drop position is specified and the light scattered onto a defined detector (position and size) is computed. The drop is then displaced in flight direction by a step distance of  $\Delta z$  and the computation is repeated. The intensity collected on the detector for each drop position is converted into a time signal using the prescribed drop velocity  $v_z$ . To obtain the time-shift signal, the light scattering of all drop positions in which incident rays intersect with the drop need to be computed.

If a flake is embedded in the drop, then the ray tracing must account for reflection on the flake surface and continue computing the path of the reflected ray. This ray may also contribute to the final intensity collected on the detector.

For validation of signal generation, simulations have been performed for the experimental results presented in [12] without a flake embedded in the drop. The essential information of the time-shift signal is not the signal amplitude, but the time difference or distance between the different signal peaks, arising from the different scattering orders. Figure 7 shows a simulated time-shift signal. The distances between the different signal peaks were measured and the gamma coefficient [12], defined in Eq. (10), was calculated. Equation (10) yields for the simulated conditions a value of  $\gamma=2.12$ . The simulation yields a value of  $\gamma=2.06$ , confirming excellent agreement.

$$\frac{\Delta d_2}{\Delta d_1} = \frac{\left[ \cos \frac{\theta_s}{2} + \sin \theta_i^{(p=2,2)} \right]}{\left[ \cos \frac{\theta_s}{2} + \sin \theta_i^{(p=2,1)} \right]} = \gamma \quad (10)$$

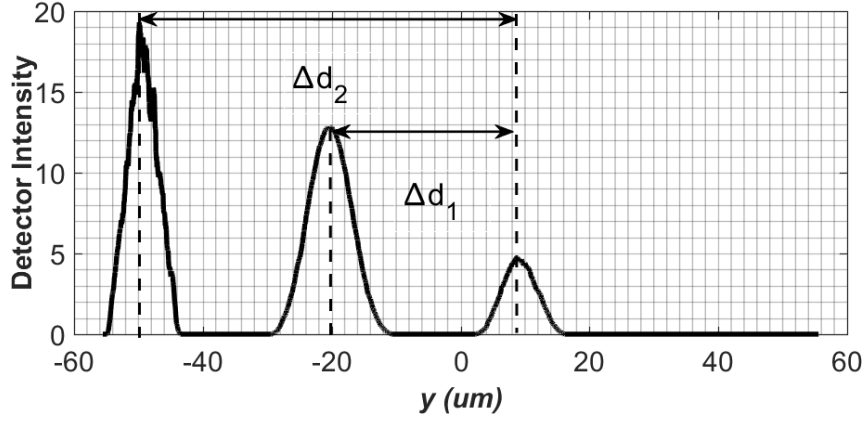


Figure 7: Simulated time-shift signal for a transparent drop:  $\theta_s=160$  deg,  $d=100\mu\text{m}$ ,  $n_t=1.36$ ,  $\Delta z=0.03\mu\text{m}$ .

## 6. Results and Discussion

After validation of the code, scattering diagrams for the drop with an embedded flake have been computed. To analyse the effect of the flake on the scattering diagram, the scattered intensity has been normalized and plotted together with the results without a flake and, additionally, compared to the Lorenz-Mie solution with Debye series decomposition. Such a comparison is shown in Figure 8 for the reflection scattering order. As expected, the embedded flake does not influence the scattering through reflection.

A similar comparison for the same drop was given in Figure 5 for first-order refraction. The scattering diagram indicates that while some of the light in forward scatter is now blocked by the flake, additional light is scattered in the backward direction. This light comes from reflection off the surface of the flake.

The same comparison is shown in Figure 9 for scattering of second-order refraction. In this case, the high intensity of the rainbow is properly captured; however, additional light is now found in the forward direction, again coming from reflection off the surface of the flake, as depicted in Figure 10a. Comparing with the scattering when no flake exists, part of the backward scattering remains the same, this can be explained with Figure 10b. In Figure 10b, the black line with arrows represents the ray path inside the drop; the dashed line shows the imaginary ray path when the drop does not contain a flake. After two further internal reflections, it is evident that the ray path and the imaginary ray path share the same exit point and exit the drop with the same angle as for second-order scattering. The blocking angle for the second-order refraction scattering can be calculated with the following equations:

$$\frac{r}{\sin \theta_t} = \frac{R}{\sin(0.5 * \pi - \sin^{-1}(\sin \theta_t * n_t) + 3 * \theta_t)} \quad (11)$$

$$\theta_b = \pi + 2 * \theta_t - 4 * \theta_t \quad (12)$$

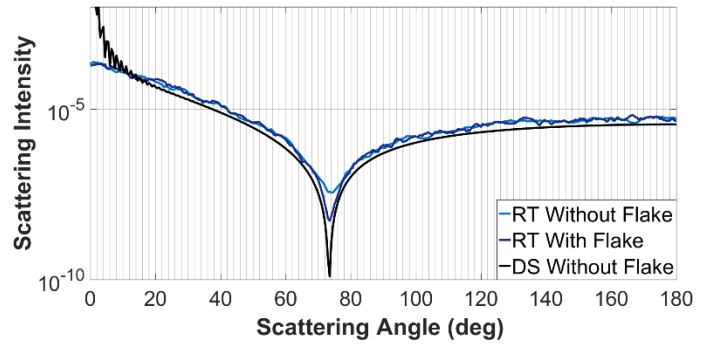


Figure 8: Comparison of the reflection scattering order ( $p=0$ ) for the parameters: drop diameter= $100\mu\text{m}$ , flake diameter= $60\mu\text{m}$ , zenith angle  $\alpha=0$  deg, azimuthal angle  $\beta=0$  deg,  $n_t=1.343$ . RT – Ray Tracing, DS – Debye Series.

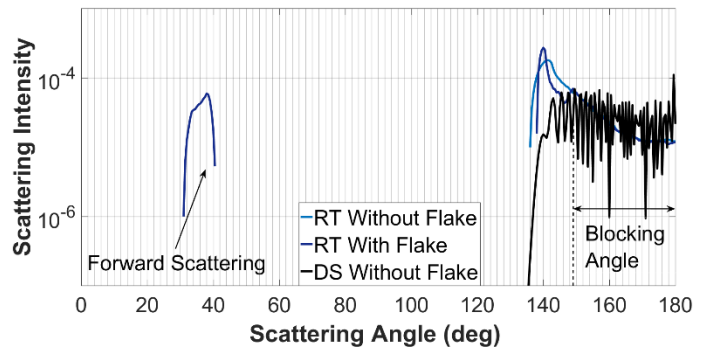


Figure 9: Comparison of the second-order refraction scattering ( $p=2$ ) for the parameters: drop diameter= $100\mu\text{m}$ , flake diameter= $60\mu\text{m}$ , zenith angle  $\alpha=0$  deg, azimuthal angle  $\beta=0$  deg,  $n_t=1.343$ . RT – Ray Tracing, DS – Debye Series.

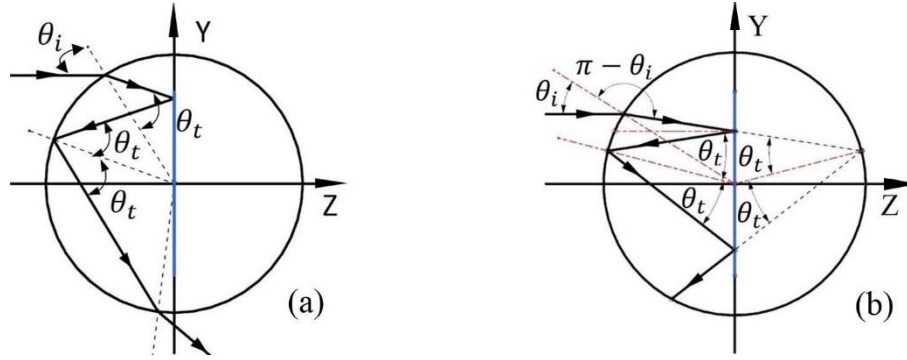


Figure 10: Ray path for second-order refraction scattering (a) Ray path for forward scattering (b) Ray path for backward scattering: drop diameter=100um, flake diameter=60um, zenith angle  $\alpha=0$  deg, azimuthal angle  $\beta=0$  deg,  $n_i=1.343$ .

The previous results were obtained using a flake azimuthal angle of 0 deg and a zenith angle of 0 deg, as depicted in Figure 4. In the following, the azimuthal angle remains at 0 deg, but the zenith angle varies from 30 deg to 90 deg with an interval of 30 deg. The embedded flake does not affect the reflection of the drop, therefore the reflection intensity at 0 deg scattering angle has been used as reference to normalize the scattering intensity from the second-order scattering. This normalized second-order scattering for different zenith angles has been plotted in Figure 11. The scattering intensity in the backscatter direction, near the rainbow, is almost unaffected by the flake. This is because most incident rays intersect with the flake twice as shown in Figure 10b.

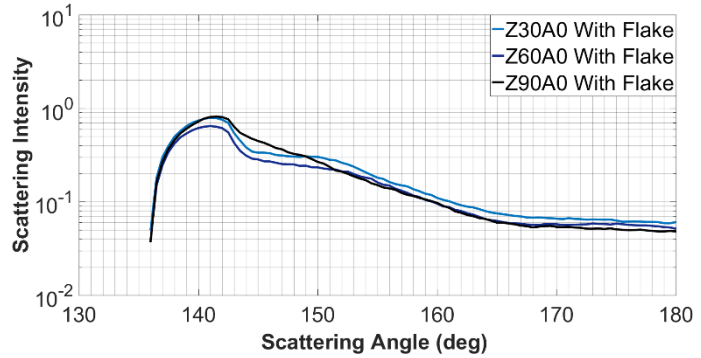


Figure 11: Second-order scattering diagram for varying zenith angle: drop diameter=100um, flake diameter=60um, azimuthal angle  $\alpha=0$  deg,  $n_i=1.343$ , Z-Zenith angle, A-Azimuthal angle.

Further scattering diagrams have been computed for zenith and azimuthal angles of 0 deg but varying the size of the flake. The flake diameter is varied from 20 um to 60 um with an interval for 20 um. Figure 12 shows the scattering diagram for first-order refraction scattering. As expected, when the flake size becomes larger, the blocking angle of the first-order scattering also becomes larger and the backward scattering becomes stronger, because of the total reflection from the flake.

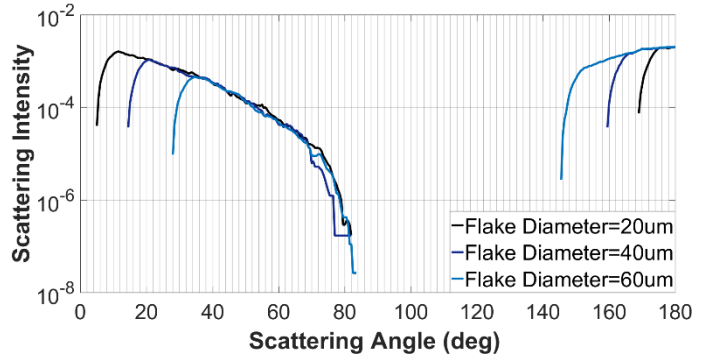


Figure 12: Comparison of the first-order scattering for different diameter of flake: drop diameter=100um, zenith angle  $\alpha=0$  deg, azimuthal angle  $\beta=0$  deg,  $n_i=1.343$ .

Figure 13 shows the scattering diagram for the second-order refraction scattering. For second-order scattering, as the flake size increases the signal from backward scattering does not change much, the reason is also that most rays intersect with the flake twice, so the rays share the same exist point and exit the drop with same angle as if no flake exists. However, changing the flake size will affect the forward scattering of the second-order scattering.

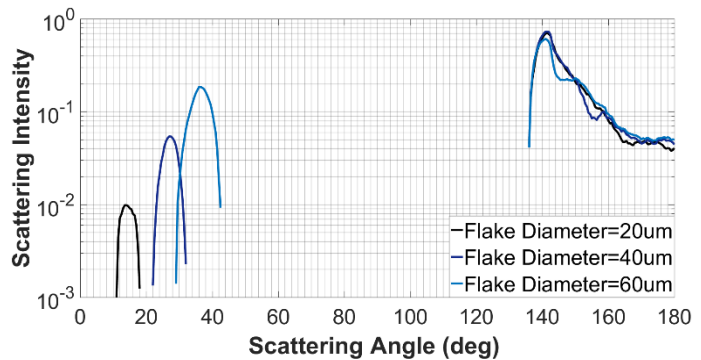


Figure 13: Comparison of the second-order scattering for different diameter of flake: drop diameter=100um, zenith angle  $\alpha=0$  deg, azimuthal angle  $\beta=0$  deg,  $n_i=1.343$ .

The total scattering diagram for varying the azimuthal angle is shown in Figure 14, when keeping the zenith angle constant. The total scattering diagrams for different azimuthal angles overlap with each other, so the total scattering amplitude does not change, when the zenith angle is constant at 90 deg and only the azimuthal angle varies.

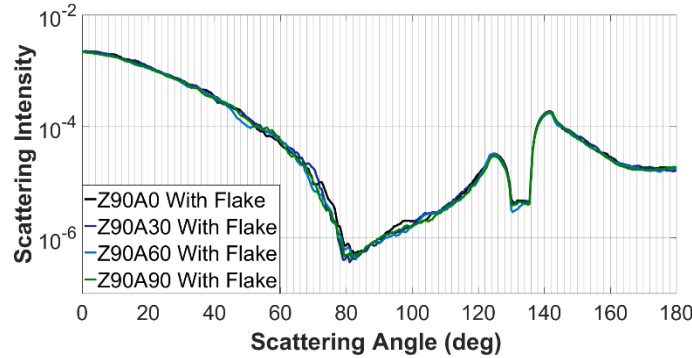


Figure 14: Total scattering diagram for varying azimuthal angle of the normal vector of the flake: drop diameter=100um, flake diameter=60um, zenith angle  $\alpha=90$  deg,  $n_i=1.343$ .

Figure 15 shows the simulated time-shift signal for the drop with an embedded flake. For comparison, the time-shift signal for a drop without a flake is also plotted; however the amplitude is almost indiscernible. Thus, when a flake is present, the corresponding time-shift signal has an extremely high intensity signal peak. This high intensity results because there is only total reflection along the ray path for the case of a flake, whereas for the pure drop, the intensity of second-order refraction decreases by the amount which leaves the drop as first-order scattering. Although the peak for total reflection from the flake is strong, the signal from reflection and second-order refraction ( $p=2.2$ ) remain the same.

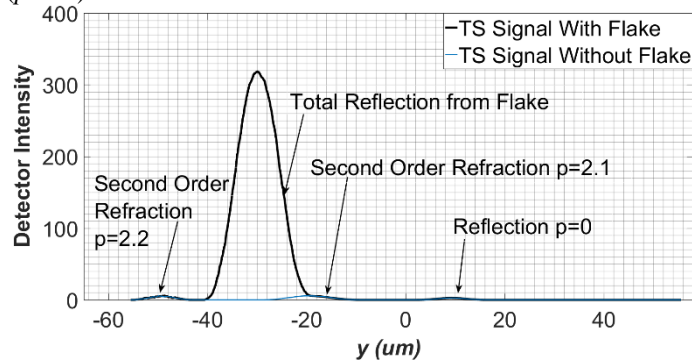


Figure 15: Simulated time-shift signal: drop diameter=100um, flake diameter=60um, zenith angle  $\alpha=0$  deg, azimuthal angle  $\beta=0$  deg,  $n_i=1.343$

## Summary and Conclusions

This study has shown how a reflecting circular flake (disk) inside a spherical drop can modify the light scattered from the drop. A ray tracing approach has been used, allowing large drops to be considered, as encountered in, for example, paint sprays. These scattering characteristics have then been invoked to simulate signals as generated by a time-shift instrument, comparing signals with and without a flake embedded in the drop. The overall aim is to explore whether the time-shift signal contains sufficient information to not only yield the size and velocity of the particle, but also whether a flake is present or not.

From the results presented, it appears as though flake identification with the time-shift technique should be possible, because when a flake is present, an additional signal peak of very high amplitude is obtained in the backscatter direction, where typically the detectors of a time-shift instrument are placed. It appears that this conjecture may be valid independent of flake size, since during passage of the drop through the measurement volume, even smaller flakes will affect the scattering diagram. It is now necessary to explore over what ranges of zenith and azimuthal angles of flake orientation a strong 'reflection' peak exists in the time-shift signal.

The next step of this study is to realize this situation in the laboratory by using a controlled flake embedment in drops of known size and to compare the obtained signals with the signals simulated in the present study.

## Acknowledgements

The authors would like to thank the Federal Ministry for Economic Affairs and Energy of Germany for financial support through the Central Innovation Programme for SMEs (ZIM), contract ZF4415101LT7. They also appreciate the cooperation of the High-Performance Computing Center of the TU Darmstadt.

## References

- [1] Albrecht H-E, Damaschke N, Borys M, Tropea C (2013) **Laser Doppler and Phase Doppler Measurement Techniques**. Springer Science & Business Media, Heidelberg
- [2] AOM-Systems, accessed April 2018, <https://www.aom-systems.com/en/category-1/sprayspy/>
- [3] Arnaud JA, Kogelnik H (1969). Gaussian light beams with general astigmatism. *Appl Opt*, **8**: 1687-1694, DOI: 10.1364/AO.8.001687
- [4] Debije (Debye) P (1908) Das elektromagnetische Feld um einen Zylinder und die Theorie des Regenbogens, *Physikalische Zeitschrift* 9:775-778
- [5] Hecht E (2001) **Optics** (4 edition), Addison-Wesley, New York
- [6] Kahnert M (2005) Irreducible representations of finite groups in the T-Matrix formulation of the electromagnetic scattering problem. *J Opt Soc Am A* **22**(6)
- [7] Kochkina (2013) Stigmatic and Astigmatic Gaussian Beams in Fundamental Mode. Ph.D. thesis. Leibniz Universität Hannover, [http://edok01.tib.uni-hannover.de/edoks/e01dh13/7\\_57170285.pdf](http://edok01.tib.uni-hannover.de/edoks/e01dh13/7_57170285.pdf)
- [8] Macke A (1994) Modellierung der optischen Eigenschaften von Cirruswolken. Ph.D. thesis, University of Hamburg.
- [9] Manfred W, Yang P (2012) **Theory of Atmospheric Radiative Transfer** WILEY-VCH, Leipzig
- [10] Mie G (1908) Beiträge zur Optik trüber Medien, speziell kolloidaler Metallösungen. *Annalen der Physik* (4) **25**:377.452
- [11] Saleh BEA, Teich MC (2007) **Fundamental of Photonics**, 2<sup>nd</sup> ed. John Wiley & Sons, Inc, Hoboken, New Jersey
- [12] Schäfer W, Tropea C (2014) Time-shift technique for simultaneous measurement of size, velocity, and relative refractive index of transparent droplets or particles in a flow, *Appl Opt* **53**:588-597
- [13] Stegmann PG, Tropea C, Järvinen E, Schnaiter M (2016) Comparison of measured and computed phase functions of individual tropospheric ice crystals", *J Quant Spectr Rad Transfer*, **178**:379-389
- [14] Sullivan DM (2013) **Electromagnetic Simulation using the FDTD Method**, IEEE Press, John Wiley & Sons, Inc., Hoboken, New Jersey
- [15] Ren K-F, Onofri F, Roze C, Girasole T (2011) Vectorial complex ray model and application to two-dimensional scattering of a plane wave by a spheroidal particle. *Opt Lett* **36**:270-2
- [16] van de Hulst H (1981) **Light Scattering by Small Particles**, Dover, New York
- [17] Yu, Haitao (2013) Laser Beam Interaction with Spheroidal Droplets: Computation and Measurement. Ph.D. thesis. TU Darmstadt, 2013. <http://tuprints.ulb.tudarmstadt.de/view/person/Yu=3AHaitao=3A=3A.html>